Study of internal lattice strain distributions in stainless steel using a full-field elasto-viscoplastic formulation based on fast Fourier transforms

A.K. Kanjarla [*], R.A. Lebensohn, L. Balogh, C.N. Tomé

Materials Science and Technology Division, Los Alamos National Laboratory, Los Alamos, NM 87545, USA

Abstract

In this work, the evolution of internal lattice strains in face-centered cubic stainless steel under uniaxial tension is studied using a recently developed full-field elasto-viscoplastic formulation based on fast Fourier transforms. The shape of the diffraction peaks is simulated, and the predicted lattice strains (peak shift and broadening) are compared with the experimental measurements obtained by in situ tensile neutron diffraction. Detailed analysis of the lattice strain distributions reveal that {100} and {110} transverse families exhibit a bimodal nature, and that transverse lattice strains are more sensitive to local grain interactions compared with longitudinal lattice strains. A comparison with the results of a mean-field formulation indicates that type III (intragranular) stresses play a much larger role than type II (intergranular) stresses in diffraction peak broadening.
Published by Elsevier Ltd. on behalf of Acta Materialia Inc.

Keywords: Lattice strains; Stainless steel; Neutron diffraction; Yield phenomena; Peak broadening

1. Introduction

Distributions of the externally applied load and stress concentration regions are topics of considerable relevance in the deformation behavior of polycrystalline aggregates. Owing to the elastic and plastic anisotropy of most polycrystal aggregates, the distribution of mechanical fields in a microstructure is rarely uniform, and macroscopic properties usually represent an average manifestation of the local micro-scale distributions. Proper understanding of them is important not only in developing materials for future applications [1,2], but also to assess the structural safety of in-service components [3,4]. Advancements in experimental capabilities now allow one to obtain the evolution of internal mechanical fields both during and after thermo-mechanical loading in a non-destructive fashion. High energy X-rays [5–7] and neutrons [8], owing to their

high penetration depth, are now used for in situ measurement of the internal stresses and strains. With neutrons, one can characterize a larger subset of material compared with the high energy X-rays. At this point, neutron diffraction is well established to measure the evolution of lattice (elastic) strains due to change in lattice spacing, from a statistically significant volume of material. Techniques using high energy X-rays are focused mostly on understanding substantially smaller material volume and at local scale with high spatial resolution of the mechanical fields [9]. The current work focuses on the in situ neutron diffraction measurement of lattice strain evolution in a stainless steel loaded in tension.

Numerical approaches to studying the lattice strains can be broadly classified into full-field methods and homogenization (mean-field) models. Crystal plasticity finite element (CPFE) formulations, capable of modeling material behavior with a realistic 3-D microstructure description, fall into the former category [10–14]. The value of full-field methods resides in that they can be tailored to render information

* Corresponding author. Tel.: +1 505 665 5960; fax: +1 505 667 8021.
E-mail address: anand@lanl.gov (A.K. Kanjarla).

on stress distributions inside grains or in the vicinity of specific grain boundaries. Such information, in turn, can be used to develop statistically based models of recrystallization, twin nucleation or fracture initiation. In contrast, homogenization models such as the elastoplastic self-consistent (EPSC) model have been extensively used to study lattice strains in materials with both cubic [8,15] and hexagonal crystal symmetries [16,17]. Taylor-type grain interaction models were also used to study the internal stress in cubic systems [18,19]. However, an inherent limitation of homogenization models is the statistical representation of microstructures, which prevents one from realistically accounting for neighboring grain interactions and intragranular (type III) stresses. Although these models do a reasonably good job at matching some experimental measurements, they cannot be used to study the influence of local variations in the microstructure. The CPFE model, however, was used to study the influence of elastic anisotropy and various grain shapes on lattice strain predictions [13,20].

This work uses a crystal plasticity fast Fourier transform (FFT) based method, which is a numerically efficient alternative to CPFE. Existing FFT-based formulations are in place for either purely elastic or purely viscoplastic materials [21,22]. This study makes use of an extended formulation that includes elasticity and viscoplasticity [23] to simulate in situ diffraction conditions and calculate the evolution of lattice strains in stainless steel. The novelty of this work is that, in addition to comparing the average lattice strains, it also analyzes their distributions. Another motivation for the present work is to establish a procedure that can be used further to benchmark hardening models based on following the evolution of dislocation densities. Note that both dislocation densities and intragranular stress fluctuations lead to diffraction peak broadening.

The outline of the paper is as follows: Section 2 briefly reviews the properties of the material studied and the lattice strain measurements. Section 3 describes the elasto-viscoplastic FFT model and the numerical diffraction procedure used in this study. Section 4 presents the results of the simulations and compares them with the experimental measurements. Section 5 discusses the numerical diffraction peaks in the context of the experimental peak broadening and the influence of local neighborhood interactions on lattice strains. A summary of the findings is presented in Section 6.

2. Material and methods

2.1. Experimental method: in situ neutron diffraction

Lattice strain measurements were conducted using the in situ neutron diffraction Spectrometer for Material Research at Temperature and Stress (SMARTS) instrument at Los Alamos National Laboratory [24]. SMARTS uses the pulsed neutron source at Los Alamos Neutron Science Center (LANSCE) for simultaneous time-of-flight

(TOF) measurements of full diffraction patterns in two detector banks oriented at ±90° to the incident beam. The samples are always oriented such that the loading direction is at 45° to the incident beam, and thus the two detector banks allow simultaneous measurements of lattice spacing along the axial (longitudinal) and transverse direction at once. This is shown schematically in Fig. 1.

2.2. Material: stainless steel

The material chosen for this particular study is an austenitic 317L stainless steel previously measured and described by Clausen et al. [25] and recently studied by Neil et al. [8]. The tensile sample was cut at 60° with respect to the rolling direction in a sheet of material which had a weak rolling texture (see Fig. 2a). The material exhibits a high Zener elastic anisotropy ratio $Z = 3.77$ (where $Z = (2 \times C_{44})/(C_{11} - C_{12})$), an initial yield strength of $\sim$250 MPa and a linear work hardening regime (see Fig. 3). The tensile specimen was loaded in the in situ diffraction instrument such that the normal direction of the sheet was aligned with the transverse scattering vector (i.e., axis 3), and the tensile direction, at 60° from the rolling direction, was aligned with the longitudinal scattering vector.

3. Numerical simulations

3.1. Elasto-viscoplastic FFT formulation

Following the seminal work of Moulinec and Suquet [26,27] on the computation of full micromechanical fields using FFT in composite materials, Lebensohn [21] extended this approach to polycrystals deforming in a rigid-viscoplastic (VP) regime. The VP-FFT formulation was successfully used to study both macroscopic and microscopic aspects of polycrystal deformation, such as prediction of global [28] and local [22] texture evolution
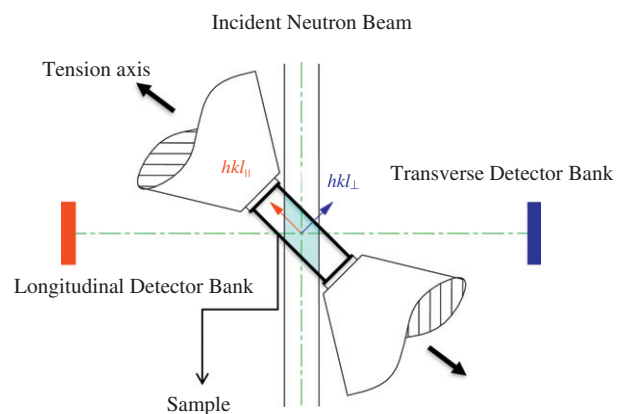

Fig. 1. Schematic of the in situ neutron diffraction at LANSCE. The grains with {hkl} planes along the loading direction diffract the incident beam to the red detector. The grains with {hkl} planes in the transverse direction diffract the incident beam to the blue detector (not to scale).
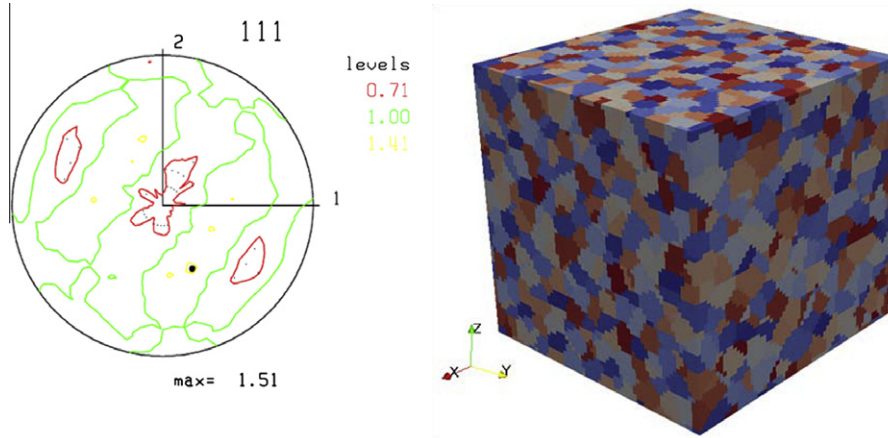
Fig. 2. Left: (1 1 1) pole figure of the initial texture. Tensile sample cut at an angle of 60° to the rolling direction. Right: realization of a microstructure with 2500 grains used in the EVP-FFT calculations. Four such realizations were used in the simulations.
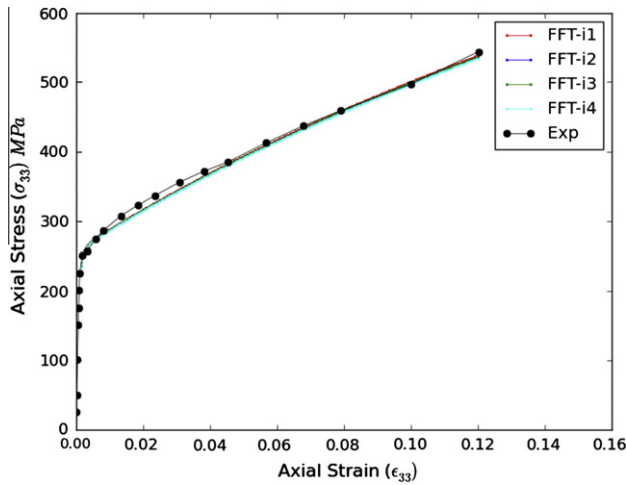

Fig. 3. Macroscopic stress–strain curve from experiments and from simulations. The only fitting procedure used in this work was to identify the Voce parameters for work hardening based on the experimental curve. Observe that the four realizations of the microstructure predict the same macroscopic response.

in cubic metals, kink-band formation in hexagonal close packed ice [29], identification of potential damage initiation sites in polycrystalline microstructures [2], to mention a few. This work makes use of the recent extension of the FFT-based formulation to the elasto-viscoplastic regime [23] for the prediction of internal stresses with intragranular resolution.

The FFT-based formulation provides a solution for periodic unit cells of the governing equations (equilibrium and compatibility). Equilibrated stress and compatible strain fields are adjusted iteratively, such that, at the same time, they fulfill the required constitutive relation. Fourier transform of Green functions of a periodic linear reference medium and convolution integrals, evaluated efficiently in Fourier space, are used to solve the micromechanical problem.

The elasto-viscoplastic FFT formulation for polycrystals is now summarized. The viscoplastic part of the strain-rate $\dot{\boldsymbol{\varepsilon}}^p(\mathbf{x})$ is constitutively related to the stress $\boldsymbol{\sigma}(\mathbf{x})$ at a single-crystal material point $\mathbf{x}$ through a sum over the N active slip systems, of the form [30]:

$$
\dot{\boldsymbol{\varepsilon}}^p(\mathbf{x}) = \sum_{s=1}^{N} \mathbf{m}^s(\mathbf{x})\dot{\gamma}^s(\mathbf{x}) = \dot{\gamma}_o \sum_{s=1}^{N} \mathbf{m}^s(\mathbf{x}) \left(\frac{|\mathbf{m}^s(\mathbf{x}) : \boldsymbol{\sigma}(\mathbf{x})|}{\tau_o^s(\mathbf{x})} \right)^n
$$
$$
\times \operatorname{sgn}(\mathbf{m}^s(\mathbf{x}) : \boldsymbol{\sigma}(\mathbf{x})), \tag{1}
$$

where $\dot{\gamma}^s(\mathbf{x}), \tau_o^s(\mathbf{x})$ and $\mathbf{m}^s(\mathbf{x})$ are, respectively, the shear rate, the critical resolved shear stress (CRSS) and the (symmetric) Schmid tensor, associated with slip system(s) at point $\mathbf{x}$; $\dot{\gamma}_o$ is a normalization factor, and n is the rate-sensitivity exponent. Owing to strain hardening, the CRSS of the slip system(s) is, in general, a function of accumulated plastic strain in the crystal, in turn a function of the stress. In order to solve the elasto-viscoplastic problem, a Euler implicit time discretization is adopted, which, combined with Hooke's law and the assumption of small strains, allows the stress in material point $\mathbf{x}$ at $t + \Delta t$ to be written as:

$$
\boldsymbol{\sigma}^{t+\Delta t}(\mathbf{x}) = \mathbf{C}(\mathbf{x}) : \boldsymbol{\varepsilon}^{e,t+\Delta t}(\mathbf{x}) = \mathbf{C}(\mathbf{x})
$$
$$
: (\boldsymbol{\varepsilon}^{t+\Delta t}(\mathbf{x}) - \boldsymbol{\varepsilon}^{p,t}(\mathbf{x}) - \dot{\boldsymbol{\varepsilon}}^{p,t+\Delta t}(\mathbf{x}, \boldsymbol{\sigma}^{t+\Delta t})\Delta t), \tag{2}
$$

where $\boldsymbol{\sigma}(\mathbf{x})$ is the Cauchy stress tensor, $\mathbf{C}(\mathbf{x})$ is elastic stiffness tensor, $\boldsymbol{\varepsilon}(\mathbf{x}), \boldsymbol{\varepsilon}^e(\mathbf{x})$ and $\boldsymbol{\varepsilon}^p(\mathbf{x})$ are the total, elastic and plastic strain tensors, and $\dot{\boldsymbol{\varepsilon}}^p(\mathbf{x})$ is the plastic strain-rate tensor given by Eq. (1). Omitting the index $t + \Delta t$, the constitutive Eq. (2) and its inverse relation read:

$$
\boldsymbol{\sigma}(\mathbf{x}) = \mathbf{C}(\mathbf{x}) : (\boldsymbol{\varepsilon}(\mathbf{x}) - \boldsymbol{\varepsilon}^{p,t}(\mathbf{x}) - \dot{\boldsymbol{\varepsilon}}^p(\mathbf{x}, \boldsymbol{\sigma})\Delta t), \tag{3}
$$
$$
\boldsymbol{\varepsilon}(\mathbf{x}) = \mathbf{C}^{-1}(\mathbf{x}) : \boldsymbol{\sigma}(\mathbf{x}) + \boldsymbol{\varepsilon}^{p,t}(\mathbf{x}) + \dot{\boldsymbol{\varepsilon}}^p(\mathbf{x}, \boldsymbol{\sigma})\Delta t. \tag{4}
$$

Adding and subtracting from the stress tensor the expression $C_{ijkl}^o u_{k,l}(\mathbf{x})$, where C_{ijkl}^o is the stiffness of reference medium and $u_{k,l}(\mathbf{x})$ is the displacement-gradient tensor, gives:

$$
\sigma_{ij}(\mathbf{x}) = C_{ijkl}^o u_{k,l}(\mathbf{x}) + \varphi_{kl}(\mathbf{x}), \tag{5}
$$

where the polarization field is given by:

$$\varphi_{ij}(\mathbf{x}) = \sigma_{ij}(\mathbf{x}) - C^o_{ijkl}u_{k,l}(\mathbf{x}) = \sigma_{ij}(\mathbf{x}) - C^o_{ijkl}\varepsilon_{kl}(\mathbf{x}). \tag{6}$$

Combining expression (5) with the equilibrium condition:

$$C^o_{ijkl}u_{k,lj}(\mathbf{x}) + \varphi_{ij,j}(\mathbf{x}) = 0. \tag{7}$$

Differential Eq. (7) is solved for a periodic unit cell under an applied strain $\mathbf{E} = \langle \varepsilon(\mathbf{x}) \rangle$ using the Green function method, i.e.

$$C^o_{ijkl}G_{km,lj}(\mathbf{x} - \mathbf{x}') + \delta_{im}\delta(\mathbf{x} - \mathbf{x}') = 0, \tag{8}$$

where $G_{km}(\mathbf{x})$ is the Green function associated with the displacement field $u_k(\mathbf{x})$. The displacement gradient is given by the convolution integral:

$$u_{k,l}(\mathbf{x}) = \int_{R^3} G_{ki,jl}(\mathbf{x} - \mathbf{x}')\varphi_{ij}(\mathbf{x}')d\mathbf{x}', \tag{9}$$

which can be solved in Fourier space, anti-transformed and symmetrized, leading to:

$$\varepsilon_{ij}(\mathbf{x}) = E_{ij} + FT^{-1}(sym(\widehat{\Gamma}^o_{ijkl}(\mathbf{k}))\hat{\varphi}_{kl}(\mathbf{k})), \tag{10}$$

where the symbol ^ indicates a Fourier transform, $\mathbf{k}$ is a point (frequency) of Fourier space, and $\widehat{\Gamma}^o_{ijkl}(\mathbf{k}) = -k_jk_l\widehat{G}_{ik}(\mathbf{k})$ is a Green operator in Fourier space, with $\widehat{G}_{ik}(\mathbf{k}) = [C^o_{kjil}k_lk_j]^{-1}$.

The FFT-based method consists in evaluating the above expressions in points and frequencies belonging to regular grids (of the same size) in Cartesian and Fourier spaces, respectively, in which case, the direct and inverse Fourier transforms in Eq. (10) become discrete, and the FFT algorithm can be applied.

Since the polarization field, defined in Eq. (6), is a function of the sought strain and stress fields, the problem should be solved iteratively. For this, an augmented Lagrangian scheme is used, adapted from Michel et al. [31,32]. If $\lambda^i(\mathbf{x})$ and $\mathbf{e}^i(\mathbf{x})$ are, respectively, auxiliary stress and strain fields at iteration (i), after some manipulation of Eq. (10), the new guess for the strain field is given by [23]:

$$e^{i+1}_{ij}(\mathbf{x}) = E_{ij} + FT^{-1}(\hat{\tilde{e}}^i_{ij} + sym(\widehat{\Gamma}^o_{ijkl}(\mathbf{k}))\hat{\lambda}^i_{kl}(\mathbf{k})). \tag{11}$$

At every material point $\mathbf{x}$, the following residual (written in contracted notation for symmetric tensors) has to be nullified:

$$R_i(\boldsymbol{\sigma}^{i+1}) = \sigma^{i+1}_i + C^o_{ij}\varepsilon^{i+1}_j(\boldsymbol{\sigma}^{i+1}) - \lambda^i_i - C^o_{ij}e^{i+1}_j = 0. \tag{12}$$

Eq. (12) is solved using a Newton–Raphson scheme:

$$\sigma^{i+1,k+1}_i = \sigma^{i+1,k}_i - \left(\frac{\partial R_i}{\partial \sigma_j}\bigg|_{\boldsymbol{\sigma}^{i+1,k}}\right)^{-1}R_j(\boldsymbol{\sigma}^{i+1,k}). \tag{13}$$

Using constitutive relations (1) and (4), the above Jacobian can be written as:

$$\frac{\partial R_i}{\partial \sigma_j}\bigg|_{\boldsymbol{\sigma}^{i+1,k}} \tilde{\simeq} \delta_{ij} + C^o_{ik}C^{-1}_{kj} + (\Delta t n\dot{\gamma}_o)C^o_{ik}$$
$$\times \sum_{s=1}^{N}\frac{m^s_k m^s_j}{\tau^s_o(\boldsymbol{\sigma}^{i+1,k})}\left(\frac{\mathbf{m}^s : \boldsymbol{\sigma}}{\tau^s_o(\boldsymbol{\sigma}^{i+1,k})}\right)^{n-1}. \tag{14}$$

In writing Eq. (14), the term $\partial\tau^s_o/\partial\sigma_j$ is neglected. Once convergence is achieved on $\boldsymbol{\sigma}^{i+1}$ (and thus on ε^{i+1}), the new guess for the auxiliary stress field $\lambda^i(\mathbf{x})$ is given by:

$$\lambda^{i+1}(\mathbf{x}) = \lambda^i(\mathbf{x}) + \mathbf{C}^o : (\mathbf{e}^{i+1}(\mathbf{x}) - \varepsilon^{i+1}(\mathbf{x})), \tag{15}$$

allowing one to start a new iteration, until correction (15) is smaller than a preset tolerance.

In the in situ neutron diffraction experiments described above, the boundary conditions are mixed, i.e., $\dot{E}_{11} > 0$, $\dot{E}_{23} = \dot{E}_{31} = \dot{E}_{12} = 0$ and $\Sigma_{22} = \Sigma_{33} = 0$ are the strain-rate and stress components imposed. To model this, the EVP-FFT algorithm should include an extra step. After $\lambda^{i+1}(\mathbf{x})$ is determined (Eq. (15)), if Σ_{pq} is one of the imposed stress components, the corresponding $(i+1)$-guess for strain component E^{i+1}_{pq} should be obtained as:

$$E^{i+1}_{pq} = E^i_{pq} + C^{o-1}_{pqkl}\alpha^{(kl)}(\Sigma_{kl} - \langle \lambda^{i+1}_{kl}(\mathbf{x})\rangle), \tag{16}$$

where $\alpha^{(kl)} = 1$ if component Σ_{kl} is imposed, and zero otherwise.

The approximate expression for the Jacobian (Eq. (14)) allows one to use different hardening laws without changing the proposed EVP algorithm. In what follows, the increase in the threshold stress with deformation (hardening) is characterized by a slip-system-based Voce law given by:

$$\tau^s_o(\mathbf{x}) = \tau^s_o + (\tau^s_1 + \theta^s_1\Gamma(\mathbf{x}))\left(1 - \exp\left(-\Gamma(\mathbf{x})\left|\frac{\theta^s_o}{\tau^s_1}\right|\right)\right), \tag{17}$$

where $\Gamma(\mathbf{x}) = \Gamma^t(\mathbf{x}) + \Delta\Gamma(\mathbf{x}) = \Gamma^t(\mathbf{x}) + \sum_{s=1}^{N}|\dot{\gamma}^s(\mathbf{x})|\Delta t$ is the accumulated shear at material point $\mathbf{x}$, $\tau^s_o, \theta^s_o, \theta^s_1, \tau^s_o + \tau^s_1$ are the initial threshold stress, the initial hardening rate, the asymptotic hardening rate and the back extrapolated threshold stress. In principle, these parameters can be different for each slip system; however, here they were chosen to be the same and obtained by fitting the experimental macroscopic stress–strain curve. The incremental change in the threshold stress is given by:

$$\Delta\tau^s(\mathbf{x}) = \frac{d\tau^s(\mathbf{x})}{d\Gamma(\mathbf{x})}\sum_{s'}h^{ss'}|\dot{\gamma}^{s'}(\mathbf{x})|\Delta t, \tag{18}$$

where $h^{ss'}$ is the hardening matrix. The incremental rotation of the crystal lattice associated with each material point can be approximated by:

$$\Delta\omega_{ij}(\mathbf{x}) = \Delta\Omega + \Delta\tilde{\omega}_{ij}(\mathbf{x}) - \Delta\omega^p_{ij}(\mathbf{x}), \tag{19}$$

where the local plastic spin is given by:

$$\Delta\omega^p_{ij}(\mathbf{x}) = \sum_{s=1}^{N}\alpha^s_{ij}(\mathbf{x})\dot{\gamma}^s(\mathbf{x})\Delta t, \tag{20}$$

with $\alpha^s_{ij}(\mathbf{x})$ being the antisymmetric Schmid tensor associated with slip system(s). In the simulations presented here, the macroscopic rotation $\Delta\Omega$ is zero, and the local fluctuation with respect to this macroscopic value is calculated as:

$$\Delta\tilde{\omega}_{ij}(\mathbf{x}) = \frac{1}{2}(u_{i,j}(\mathbf{x}) - u_{j,i}(\mathbf{x})) - \frac{1}{2}(u^t_{i,j}(\mathbf{x}) - u^t_{j,i}(\mathbf{x})). \tag{21}$$

In the current version of the code, no morphology update is performed. All the calculations are done on the fixed undeformed grid. Efforts towards updating the morphology are currently under way.

3.2. Simulation details

A realization of a microstructure is achieved by constructing a periodic unit cell discretized into a regular numerical grid of $64 \times 64 \times 64$ (262,144) material points or voxels. The numerical grid was partitioned into 2500 grains (with an average of 105 voxels per grain) by Voronoi tessellation. The initial crystallographic orientations assigned to each of these grains, were chosen such that they are statistically representative of the experimental texture [33]. Four such realizations were constructed using different initial seeds for the Voronoi tessellations. It is necessary to note that all the unit cells had same initial texture and number of grains, but different grain topologies. As a consequence, the initial sampling of the orientations representative of the experimental texture would also differ from realization to realization. The unit cells were then subjected to uniaxial tension up to 12% strain in a total of 150 steps with a strain rate of 0.0008 s^{-1}. The material parameters used for the FFT calculations are given in Table 1. A simple isotropic hardening matrix ($h^{ss'} = 1, \forall ss'$) was used.

For the sake of completeness, and because it is used for comparison with EVP-FFT, relevant aspects of the EPSC model of Turner and Tomé [34] are highlighted here. In EPSC, each grain from a polycrystal is treated as an ellipsoidal inclusion surrounded by a homogenized equivalent medium (HEM), the mechanical response of which is the volume average over all grains in the polycrystal (further details and the extension of EPSC to account for lattice rotations used in what follows can be found in Neil et al. [8]). In the context of the present study, it is important to note that in EPSC: (i) deformation and orientation fields inside the grains are homogeneous, i.e., no type III or intra-granular fields are accounted for; (ii) the near-neighbor interactions are not explicitly accounted for. The inclusion only interacts with the HEM, and its response has to be interpreted as representing the average response of all grains with the same orientation but different neighborhoods. For the current study, 23,328 discrete orientations were used to represent the initial material in EPSC.

3.3. Numerical diffraction

An hkl diffraction peak is produced by scattering from material points satisfying the Bragg condition for that particular reflection, i.e., crystals which have a common hkl plane normal closely aligned with the scattering vector (the bisector of the incident and diffracted beams). The set of contributing crystals is referred to as the hkl family for that particular scattering direction. This is achieved by first identifying the set of all crystallographically equivalent planes for general hkl indices and then calculating the dot product between the plane normal and the scattering vector. The scattering vector is given by the alignment of the specimen with respect to the detectors and the incident beams (Fig. 1). In the current work, the scattering vectors q_i are $(0,0,1)$ and $(1,0,0)$ for longitudinal and transverse strains, respectively. The hkl plane normal in the sample reference frame is given by $n_i^s = R_{ij} n_j^c$, where R_{ij} is the transformation matrix associated with the crystallographic orientation of the crystal at a voxel. If the angle θ between q_i and n_i^s less than the tolerance, the voxel contribution belongs to that particular hkl family. A tolerance of $\pm 6.5°$ was used in the current study, consistent with the span of the SMARTS detectors. Although these voxels share a plane normal, they do not necessarily have the same crystal orientation. Once the hkl family with normal n_i^s is identified, the lattice strains are calculated by normal projection of the elastic strain tensor as follows:

$$\varepsilon^{hkl} = n_i \varepsilon_{ij}^{el} n_j. \tag{22}$$

Volume averaging over all the voxels of the family gives the average lattice strain of a given hkl plane.

4. Results

FFT-based simulations of the tensile deformation of the stainless steel sample were performed using the four realizations of the initial microstructures. The rate-sensitive crystal plasticity (Eq. (1)) was used as the local constitutive relation, assuming glide on the 12 $\{111\} \langle 110 \rangle$ systems as the active slip mode, and a viscoplastic exponent $n = 20$. The initial distribution of CRSS was assumed to be uniform. The extended Voce law hardening parameters adjusted to match the experimental macroscopic stress–strain curve measured during the tensile deformation of the stainless steel sample are listed in Table 1. The experimental and simulated stress–strain curves are shown in Fig. 3.

Fig. 4a shows the evolution of longitudinal lattice strains along the three hkl planes under consideration, as measured by the in situ neutron diffraction. Also included are the predictions from the EVP-FFT model (plotted here are the ensemble average over four different realizations of initial microstructure) and the EPSC predictions. There is a good match between the model predictions and the experimental measurements. The $\{111\}$ family exhibits close to linear behavior from the elastic to the plastic regime, with very little change in the slope at the elasto-plastic transition. However, there is a clear difference in the behavior of $\{110\}$ and $\{100\}$ planes with the onset of plasticity.

Table 1
Elastic and plastic material parameters used in the current study, in MPa.

	C_{11}	C_{12}	C_{44}	τ_0^s	τ_1^s	θ_0^s	θ_1^s
FFT	204,600	137,700	126,200	102	56	375	170
EPSC	204,600	137,700	126,200	93	56	375	170

The {100} family, being elastically compliant, tends to yield first and deform plastically, thus transferring the external load to the relatively stiffer {110} and {111} families. The same is shown in Fig. 5a, where the stresses along the loading direction averaged over the corresponding *h k l* family (as calculated by EVP-FFT) are plotted against the macroscopic applied stress. It is clear that the elastically stiff {111} family carries most of the stress, and the compliant {100} family the least. For example, at an applied stress of 300 MPa, the stress in {111} family is ~80 MPa more than the {100} family. Also important to note is that predictions from both the EVP-FFT and EPSC capture the measured lattice strains very well. It appears that taking only intergranular stress fields into account is sufficient to capture the average response of individual peaks, as seen in Fig. 4a.

The evolution of transverse lattice strains is shown in Fig. 4b. As in the longitudinal case, the {111} family exhibits a stiffer response compared with the {100} family. Since the initial texture of the material is close to random, this behavior is expected: the *h k l* family stiff in longitudinal direction is also stiff in the transverse direction. Similar observation was made by Oliver et al. [35] albeit for the body centered cubic phase in duplex steel. Unlike the longitudinal families, the difference in load bearing is relatively less in the case of transverse families. As shown in Fig. 5b, at a macroscopic applied stress of 300 MPa, the difference in the stress along {111} and {100} families is ~50 MPa. The {100} family exhibits dramatic behavior with the onset of plasticity. At the elasto-plastic transition, the load transfer leads to a reversal of compressive stress and eventually starts accumulating compression with fully developed plasticity. Both the models are able to capture the general experimental trends; however, there are some obvious differences. The predictions from EVP-FFT improve upon those from EPSC in {111} lattice strains. In the case of {100}, EVP-FFT overpredicts the compressive response, while EPSC underpredicts it.

The lattice strains measured and reported in the previous section represent the average shift in the center of the peak position with respect to an unstrained reference value. Previous studies, with the exception of Dawson et al. [36] and Neil et al. [8], focused only on the first moment (average) of lattice strain distribution, with little attention paid to the distribution itself. Neil et al. [8] reported the distributions and dispersions obtained by the EPSC model. In spite of the large number of total grains (~23,000) considered, owing to the strict assumption of homogeneous strain fields inside the grains, they found that the lattice strain distributions associated with each peak were discontinuous and multimodal in nature. Dawson et al. [36] also studied the distribution of the lattice strains in aluminum and stainless steel. However, they explicitly assumed that the peaks are symmetric and compared the standard deviation of the distributions. In the EVP-FFT calculations, 2500 grains discretized by $64 \times 64 \times 64$ material points were used, thus allowing for the development of intragranular fields. The strain distribution curves obtained from one of the EVP-FFT realizations are shown in Fig. 6. The distributions are normalized histograms, where a bin size of 75 microstrains was used. In the case of longitudinal strains, the distributions are close to Gaussian and symmetrical. With increasing strain level, the spread of the distributions also increases, but not necessarily at the same level for all families. While {110} and {111} families exhibit an almost identical change in their spreads, the {100} family shows a much larger change in the spreads with deformation (see Table 2). For transverse strains, one sees more interesting trends. The {111} transverse family has regular Gaussian distribution, which is maintained with further straining. However, the {100} and {110} families exhibiting an initial Gaussian distribution quickly lose the symmetry and evolve into a bimodal distribution with relatively distinct local peaks.

To investigate further the bimodal nature of the {100} and {110} transverse peaks, the crystallographic orientation of the material points contributing to a peak was examined. Fig. 7 shows the longitudinal and transverse inverse pole figures (IPF) for those voxels that contribute to the {100} transverse peak and {110} transverse peak, at 0.25% strain and 12% strain. The location of the point in the standard stereographic triangle indicates the crystallographic axis along the chosen macroscopic axis, and the color at the point indicates the magnitude of the *h k l* component of the lattice strain. As expected for the transverse IPF, all the points are clustered around the 100 or the 110 corners, since these are the points contributing to the {100} and {110} transverse peaks, respectively; on the longitudinal IPF, there is no preferred orientation. What is perhaps more interesting is the dependence of the normal strains on the crystallographic axis along the longitudinal direction. Crystals with ⟨100⟩ parallel to the stress axis are in transverse compression, while those with ⟨110⟩ parallel to the stress axis are in a transverse tensile state. Similar trends are also seen in the case of {110} peaks.

5. Discussion

Diffraction peaks from a strained crystal lattice exhibit two main differences from those obtained from "unstrained" or reference crystal lattice: (i) lateral shift in the peak center; and (ii) broadening of the peak (see Fig. 8). The former is due to the change in the lattice plane spacing associated with type I (macroscopic) and type II (intergranular) stresses, and the latter is due to, among other factors, the fields associated with forest and geometrically necessary dislocations arising from the plastic activity in the crystal, and intragranular stress gradients associated with local accommodation (type III stresses). Patterns obtained by neutron diffraction contain information about both the above-mentioned effects. Earlier, the predicted lattice strains were compared with those obtained experimentally. The fact that stresses associated with broadening average to zero helps explain why formulations
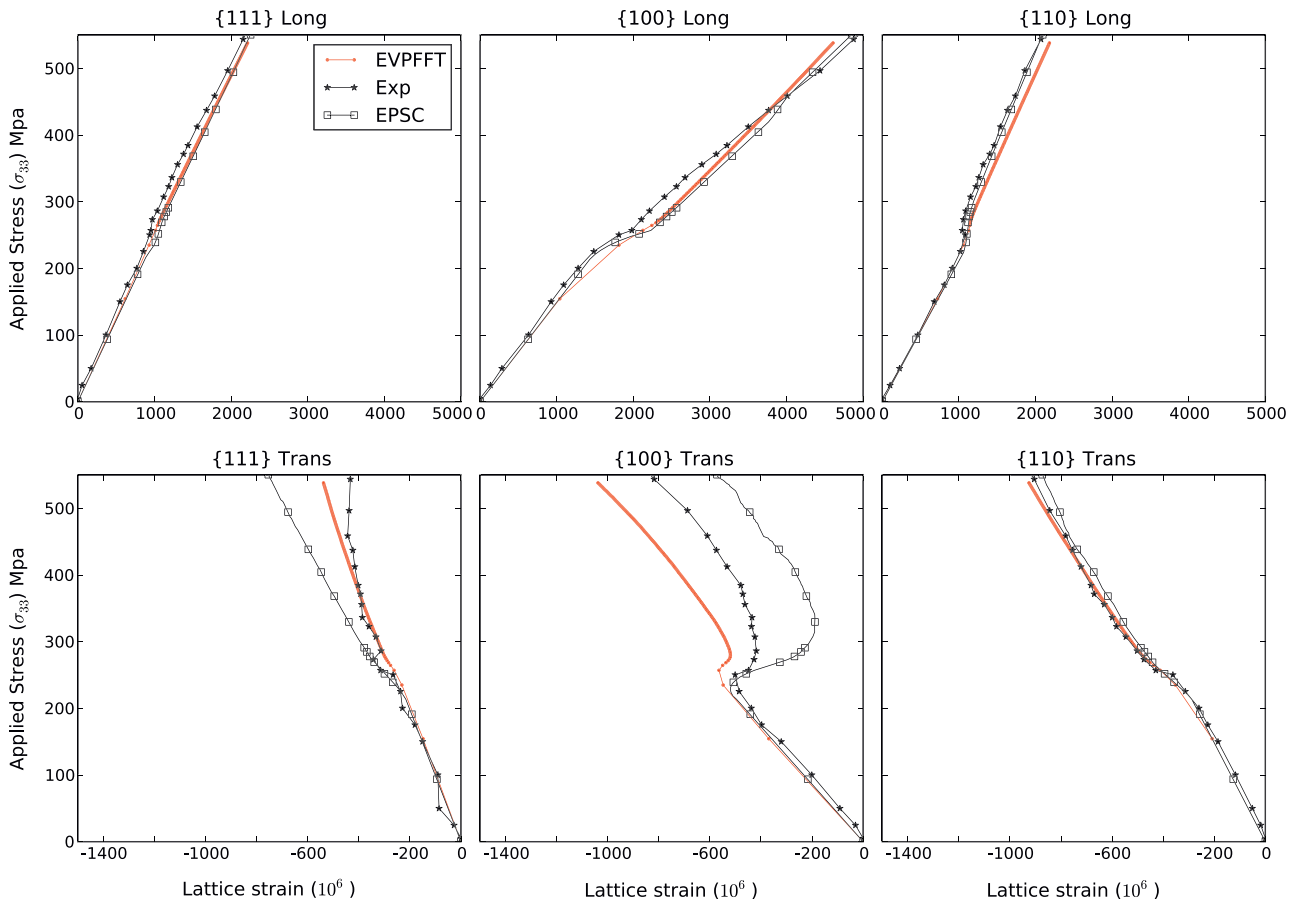
Fig. 4. Evolution of the {100}, {110} and {111} lattice strains as measured and as predicted by EVP-FFT and EPSC. The FFT results are ensemble averages over the four different microstructures used: (a) longitudinal; (b) transverse lattice strains.

that do not account for type III stress (such as EPSC) are still effective at capturing average peak shifts correctly. In this study, the distributions of the lattice strains of simulated diffraction peaks were analyzed to gain insight into the orientation dependence of the crystal behavior, and

to understand better the limitations and possibilities of the EPSC and EVP-FFT approaches.

The shape of the peak and its broadening are determined both by the microstructure of the sample and by the characteristics of the diffraction instrument, and are
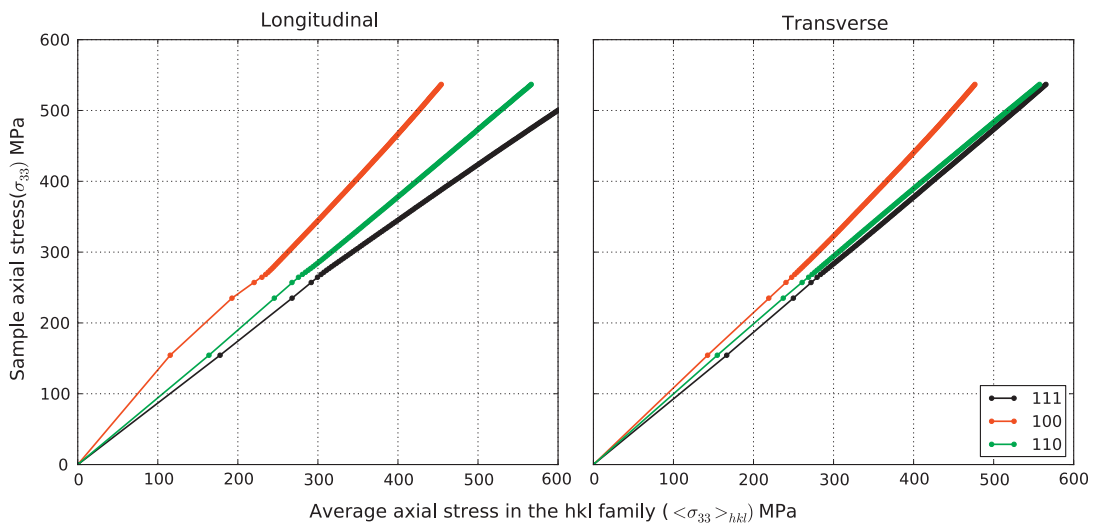

Fig. 5. Evolution of axial stresses in individual {hkl} families as calculated by EVP-FFT.
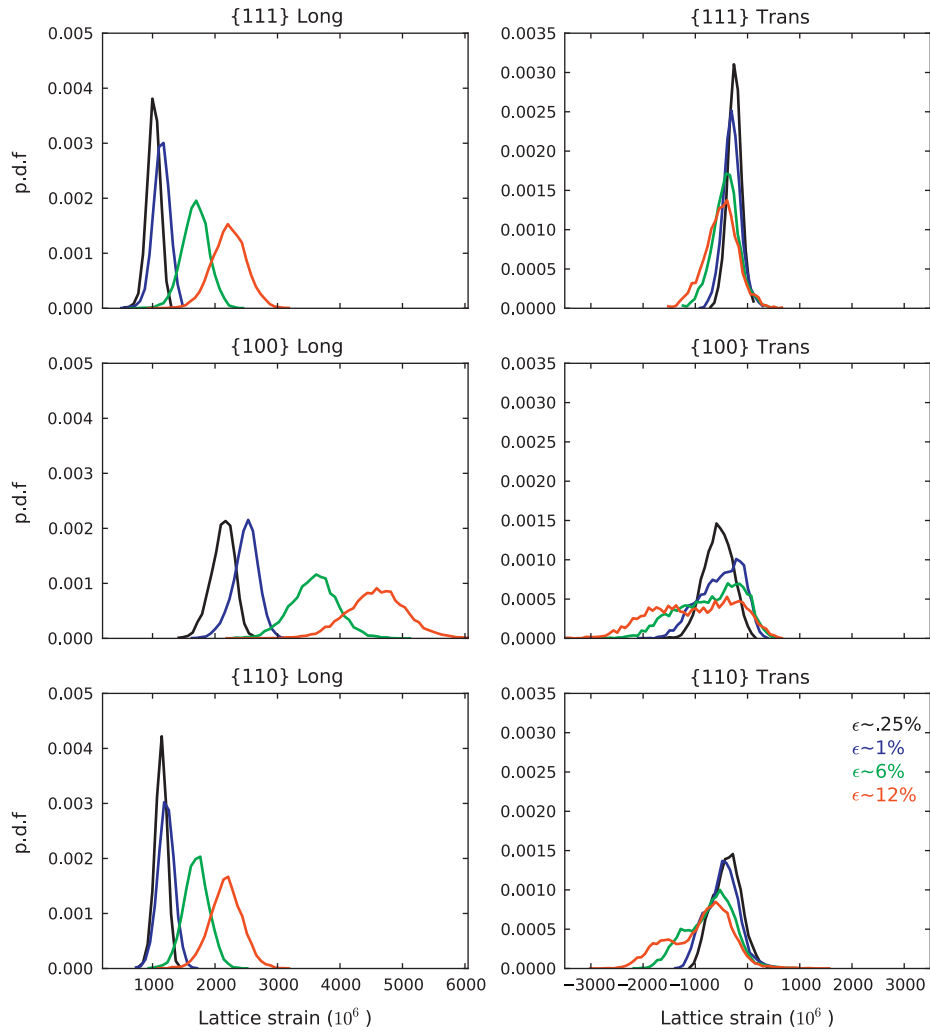
Fig. 6. Evolution of the lattice strain distribution in the individual {hkl} families as calculated by EVP-FFT. Longitudinal distributions maintain their symmetry with straining. In the case of {100} and {110} transverse, initial symmetric distributions develop a bimodal character. Distribution shown here are at 0.25%, 1%, 6% and 12% strains.

Table 2
Statistical information of the lattice strain distributions of different diffraction peaks.

| Strain (%)	No. of voxels	Mean	Standard deviation	No. of voxels	Mean	Standard deviation
	{111} Longitudinal			{111} Transverse		
0.25	7729	1015.51	103.55	3963	−253.27	132.42
1.0	7751	1140.89	130.41	3683	−300.04	174.99
6.0	10,028	1686.85	210.51	3508	−417.37	256.90
12.0	13,423	2224.69	273.14	3220	−505.13	320.31
	{100} Longitudinal			{100} Transverse		
0.25	4601	2121.09	185.01	4634	−560.63	269.69
1.0	4649	2489.47	202.88	4845	−509.51	411.14
6.0	5499	3588.23	367.53	4566	−707.98	611.32
12.0	7007	4584.85	476.77	4054	−1011.79	794.71
	{110} Longitudinal			{110} Transverse		
0.25	9385	1133.85	95.68	12,037	−396.94	268.39
1.0	8884	1214.39	131.37	12,296	−484.26	314.71
6.0	6107	1701.75	199.88	13,458	−708.22	456.29
12.0	4157	2176.39	260.71	14,891	−895.48	588.89
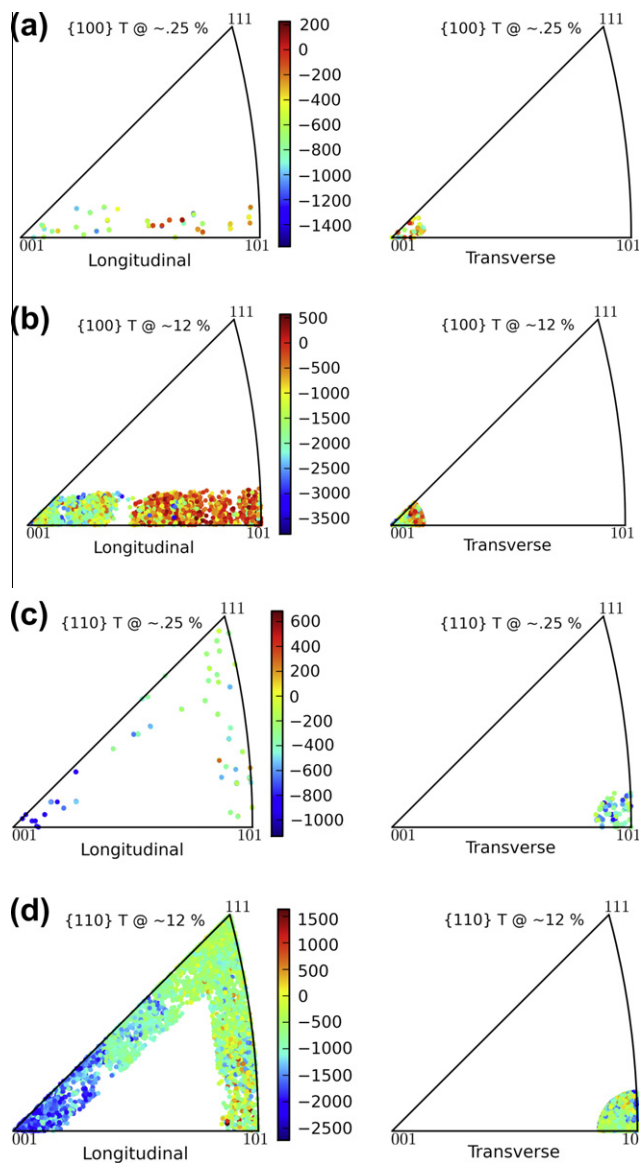
Fig. 7. Strain inverse pole figures. The position of the point indicates the crystallographic axis along the macroscopic direction and the color the lattice strain. (a and b) {100} transverse family at 0.25% and at 12% strain; (c and d) {110} transverse family at 0.25% and at 12% strain. In both cases, the 100 region of the IPF with low Taylor factor exhibits most compression and the 110 and 111 regions relative tension.
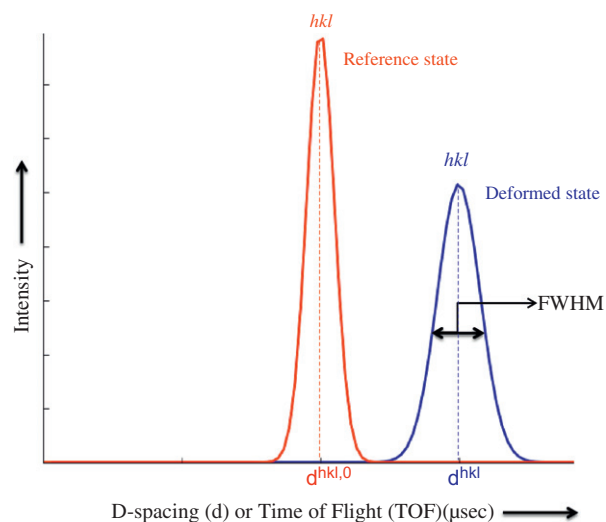

Fig. 8. Effect of deformation on a given hkl diffraction peak. Shift of the peak center is related to the lattice strains, and the change in the FWHM or peak broadening is mostly associated with related to defect accumulation.

luted from the measured peak profiles to obtain the true physical peak shapes characteristic of the microstructure of the sample [41].

In the present case, the instrumental patterns for SMARTS were collected using heat-treated, undeformed stainless steel samples with large grains and very low lattice distortion. The instrumental line profiles were deconvoluted from the measured ones using Convolutional Multiple Whole Profile diffraction line profile analysis software [38]. The numerical deconvolution performed on the stainless steel diffraction patterns shows that, in the present case, the measured broadening is the quadratic sum of the instrumental and physical broadenings with ±3% precision. Thus the physical broadening of the stainless steel line profiles, in terms of the full width at half maxima (FWHM) can be calculated as follows:

$$\text{FWHM}_{physical} = \sqrt{\text{FWHM}_{measured}^2 - \text{FWHM}_{instrumental}^2}.$$

(23)

Assuming that the measured peaks are Gaussian, the relationship between the FWHM and the standard deviation (SD) of the peak is given by $\text{FWHM} = 2\sqrt{2\ln 2}\text{SD}$.

Fig. 9 shows the standard deviation of the peaks as measured and after removing the contribution from the instrument broadening (the procedure to relate FWHM in terms of local lattice strains is described in the Appendix A). There are two clear differences: (i) the standard deviations of the peaks after removing the contribution from instrument broadening are systematically smaller than as measured, much more so at low strains (about four times); (ii) instrument broadening affects different hkl peaks in different ways. Also shown in Fig. 9 is the evolution of the standard deviation of the lattice strain distributions from the numerical simulations. While experimental and simu-

often used to obtain information about the diffracting microstructure, such as the dislocation densities and their character and grain sizes [38–40]. In the case of most diffraction equipment, the instrumental effect on the broadening and the shape of the line profile is non-negligible. The instrumental broadening is superposed with the physical broadening, and the convolution of the two is present in the final diffraction pattern. The instrumental shape and broadening can be measured using samples which do not cause any detectable physical broadening, typically large-grained, strain-free standard powders, such as LaB_6 or Si. Knowing the instrumental effects caused by the instrument, the instrumental peak shapes can be numerically deconvo-
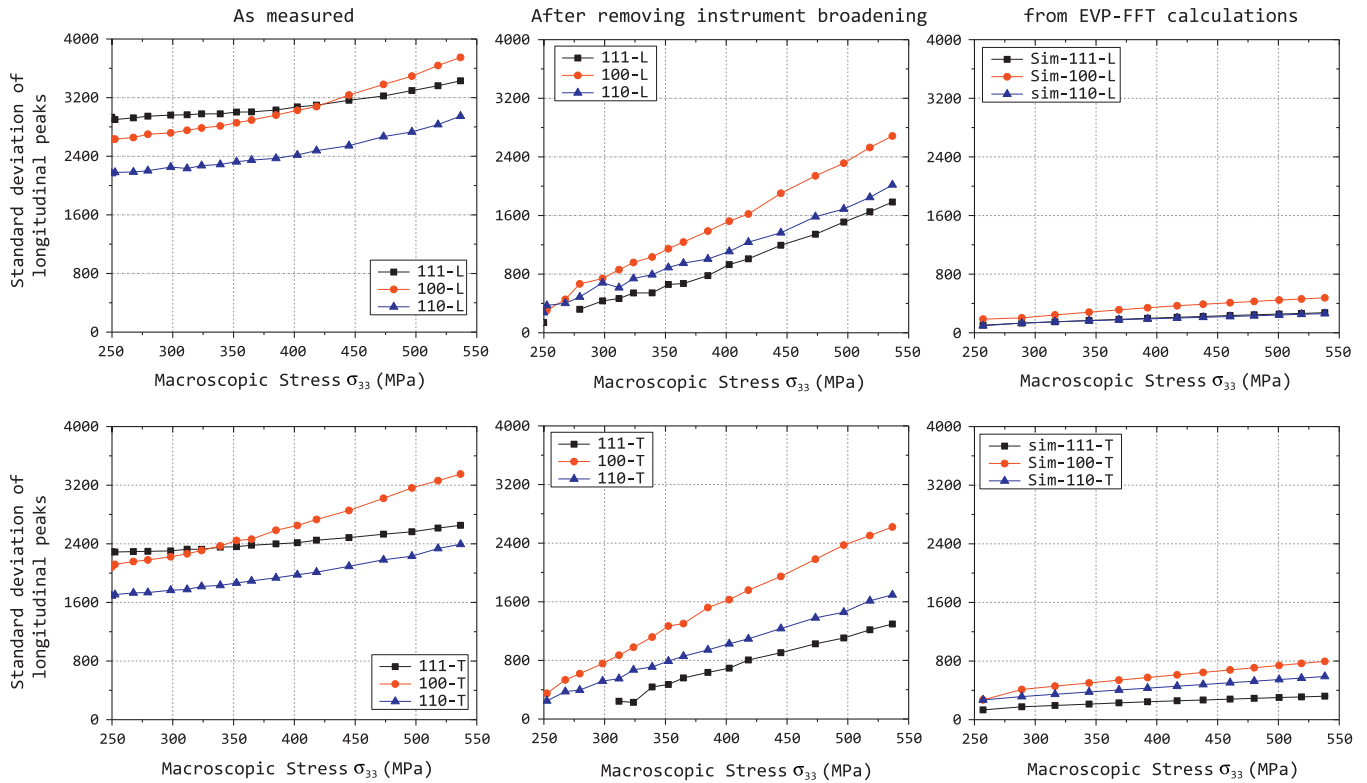
Fig. 9. Evolution of standard deviation of the peaks as measured and after deconvoluting instrument broadening. Also included are the predictions from EVP-FFT simulations: top row, longitudinal; bottom row, transverse.

lated deviations increase about linearly with strain, there is a marked difference in their magnitude, with the simulated ones being three to five times smaller. The immediate implication of this result is that it is not possible to use experimental broadening as a way to benchmark local plasticity models of polycrystals. The reason for the discrepancy requires some explanation. Physical broadening, as indicated earlier, is a combination of various factors: crystallite size broadening, micro-strain broadening arising from individual dislocations and non-uniform lattice distortion broadening. In the case of the EVP-FFT simulations, the broadening is due to the heterogeneous stress fields, because of grain interaction and the development of the intragranular misorientations. The results from the calculations correctly predict the order of the hkl peaks. In both, longitudinal and transverse, directions {100} peaks exhibit most broadening, followed by {110} and {111} peaks.

It is appropriate to discuss at this point the earlier work by Dawson et al. [36] on lattice strain distributions. These authors performed CPFE simulations on AL6XN stainless steel and Al 5182 alloys, both of cubic crystal symmetry, and report observations similar to those made here: the {100} transverse family exhibits larger standard deviations and higher broadening compared with the {100} longitudinal, contrary to what was seen experimentally. Another important aspect is the coefficient of variation (CV), i.e., the ratio of the standard deviation to the mean. In this study, it is seen that, for various longitudinal families, they

are in the range 0.08–0.12. However, for transverse families, they are substantially higher and range from 0.45 to 0.65. Careful study of Figs. 10 and 11 from Dawson et al. [36] reveal a similar range for the longitudinal case. The transverse families appear to have a much higher CV; for example, at ~12% strain, the CV for the {100} transverse family is close to 1.0. The higher values could perhaps be explained by the way in which Dawson et al. [36] performed the simulations. In their CPFE computations, each element was considered as a single crystal, a configuration that can be expected to lead to strong stress variations from element to element. In contrast, in the current work, both type II and type III stresses are allowed to evolve. Surprisingly, it appears that, by allowing for intragranular stresses, the predicted broadening is reduced. It is worth emphasizing here that the chemistry and mechanical properties of AL6XN stainless steel used by Dawson et al. [36] are different from those used here.

It is necessary to point out that the micro-strains contribution from dislocation networks is missing from the simulated peaks. This is because, in the material constitutive law used here, the behavior of individual dislocations is not explicitly taken into account. Rather, shear deformation is described by the collective behavior of a population of dislocations on a slip system, homogenized in space and time, using a simple power law and resolved shear stress for that system. This is an inherent limitation of the commonly used continuum crystal plasticity approach. To get realistic

peak broadening, the stress fields associated with individual dislocations need to be taken into account, which is currently possible by three-dimensional dislocation dynamics. However, it should be noted that current dislocation dynamics approaches cannot deal with polycrystals [42]. It is possible, though, to improve the current empirical Voce hardening with dislocation-density-based hardening laws for slip capable of coupling the excess dislocation density arising from lattice curvature/gradients to the slip resistance on a given system. Work in this direction is currently being pursued.

Another interesting aspect of the simulated peaks is the bimodal nature of the {100} and {110} transverse peaks, coming from contributions of grains within an {hkl} family, but having different overall orientation. The spatial resolution of the existing neutron diffractometers cannot resolve the contribution to the peak of individual grains. One way to obtain such information experimentally is to use high energy synchrotron X-rays to measure the elastic strains from individual grains in a polycrystal. The latter was done by Lienert et al. [37] for copper, where they followed the {110} lattice strain evolution in 20 bulk grains. However, obtaining the elastic strain tensor from a statistically significant grain population is not yet a routine proce-

dure in the three-dimensional X-ray diffraction experiments.

The response of a material point in a microstructure is influenced not only by its crystallographic orientation, but also by its immediate neighbors [43–45]. It is well established that statistical models aimed at predicting macroscopic deformation textures and plastic anisotropy perform much better by accounting for neighboring grain interactions [46,47]. In this work, the effect of neighboring interactions was studied by performing the FFT calculations on different realizations of the initial microstructure, keeping the initial texture of the material the same. This allowed a grain to be considered embedded in a different local neighborhood in each of the realizations. If there is a strong dependence on the local neighborhood, the response from each realization would be significantly different. It is seen that the macroscopic stress–strain response (Fig. 3) is insensitive to the realizations, and so are the calculated longitudinal lattice strains (Fig. 10). In the case of transverse lattice strains, the predicted lattice strains show non-negligible spread, more so in the case of the elastically compliant {100} transverse family. This is consistent with the fact that a compliant grain usually feels the effect of a neighboring grains more compared with a stiff one.
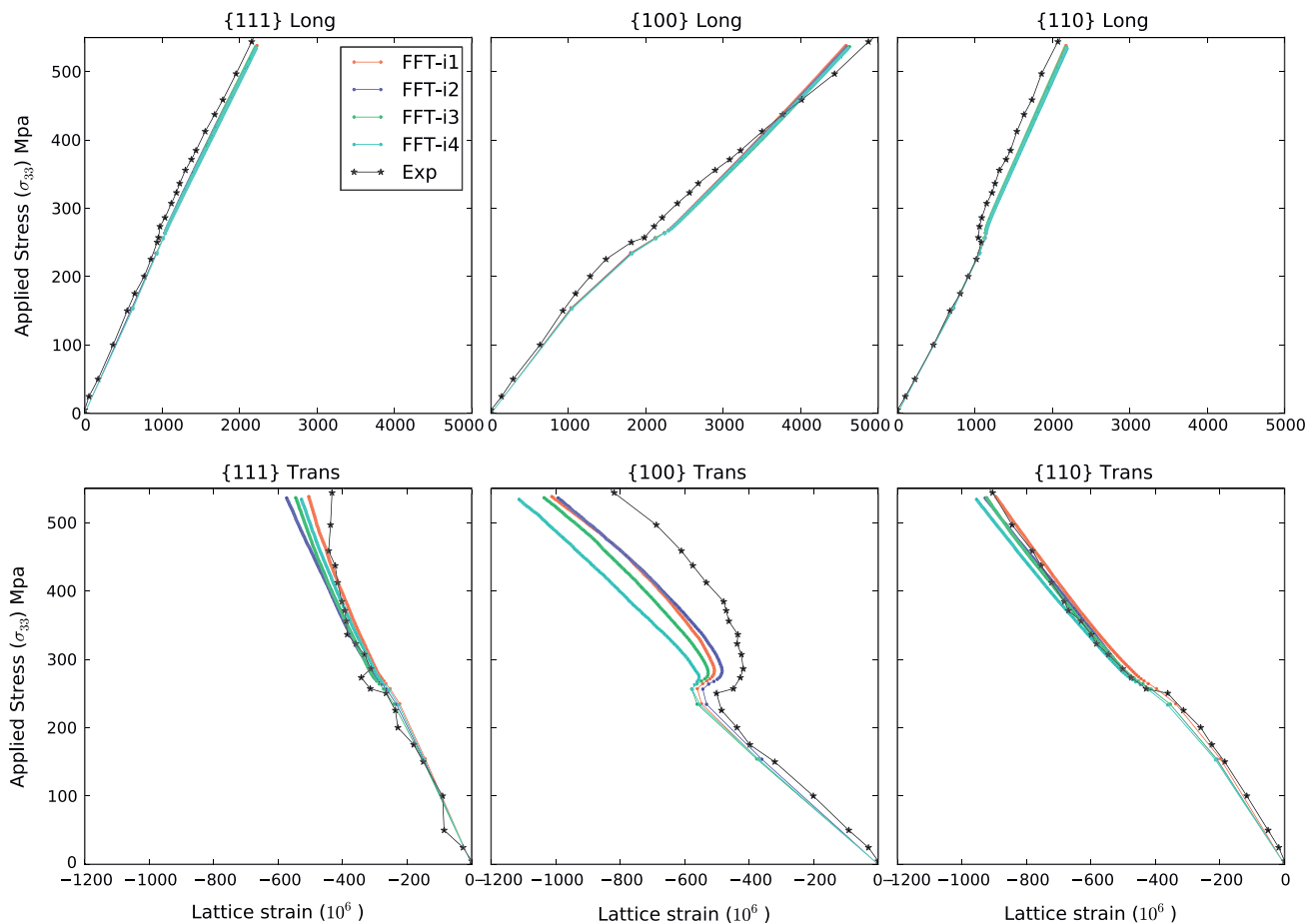

Fig. 10. Spread in lattice strains arising from different realizations used in the EVP-FFT calculations. The local surrounding or neighboring grain interactions appear to affect the transverse strains more than the longitudinal ones, particularly for the {100} transverse family.

6. Concluding remarks

In the present work, a full-field elasto-viscoplastic FFT-based formulation was introduced to solve the local mechanical fields in a polycrystal as a numerical alternative to the more traditional and numerically intensive finite element approach. The new model was used to study the internal lattice strain development in stainless steel and compared with those measured experimentally using TOF neutron diffraction.

Concerning average peak shifts, the use of different realizations of microstructures as input for the FFT simulations determined that the transverse lattice strains are more sensitive to the local neighborhood interaction (particularly the {100} transverse strains) than the longitudinal lattice strains. Overall, however, details of the neighbor configuration seem to play a secondary role in influencing the strain distribution, at least in this cubic structure. Good agreement was observed for longitudinal lattice strains and for the {111} and {110} transverse lattice. In the case of {100} lattice strains, although the EVP-FFT model shows improvement over the EPSC model, the predictions do not match the experimental measurement quantitatively.

Concerning lattice strain distributions, the present study shows that full-field simulations predict a broadening three to five times smaller than the experimental one, a fact that the authors attribute to the effect of local dislocation fields on peak broadening, not accounted for in the model. However, the results show that accounting for intragranular (type III) stresses represents an improvement of about one order of magnitude with respect to the dispersion predicted with a mean-field model, where only intergranular (type II) stresses are considered. In addition, the present study reveals that, for {110} and {100} transverse families, the distribution is non-symmetric and bimodal in nature. Plotting the crystallographic orientations of the material points contributing to the {100} transverse family revealed a strong correlation between the crystallographic axes along the loading direction. Crystals with ⟨100⟩ along the loading direction were in relative compression compared with those with ⟨110⟩. As for the relation between broadening and the details of the grain neighborhood, no significant differences were observed between different realizations. The largest corresponds to {100} transverse strains, and is associated with a large reversal effect during the elasto-plastic transition.

Table A1
Diffraction instrument constants used in the current study.

Detector	DIFA ($\mu s\ A^{-2}$)	DIFC ($\mu s\ A^{-1}$)	ZERO (μs)
Bank2-longitudinal	0.91	13040.40	6.08
Bank1-transverse	4.46	13027.50	10.65

Appendix A. Estimation of the peak broadening in terms of lattice spacing (strain) from TOF neutron diffraction measurements

The broadening of a diffraction peak is commonly characterized by the FWHM. This appendix describes how FWHM is estimated in terms of the change in lattice spacing (local microstrains) for measurements performed at SMARTS.

In TOF neutron diffraction measurement, a short pulse of neutrons with varying wavelengths is incident on a sample. Neutrons of a given wavelength are diffracted by lattice planes for which Bragg's condition is satisfied. Further, since the kinetic energy and hence the velocity of neutrons is dependent on the wavelength, they arrive at the detector at different times. The time taken to reach the detector bank from the source is recorded and is known as time of flight [48]. For the diffracted neutron, the relationship between the time TOF^{hkl} in microseconds and the d-spacing of a reflection (d^{hkl}) in angstroms is given by

$$TOF^{hkl} = DIFA \times (d^{hkl})^2 + DIFC \times d^{hkl} + ZERO. \quad (A1)$$

In the above equation, DIFC (diffraction constant) is the linear proportionality constant related to the experimental setup of the diffractometer, specifically the distances between the neutron source, the sample and the detector. DIFC varies from one detector bank to another; therefore, the values for the longitudinal and transverse detectors are different. DIFA (diffraction absorption) is related to the neutron absorption cross section. And ZERO is an instrument constant. Further details can be found in Ref. [49]. The values of the constants used in the current study are given in Table A1.

The FWHM for an hkl peak in terms of lattice strains is given as follows

$$FWHM^{hkl} = \frac{\Delta TOF^{hkl}}{d_o^{hkl}\sqrt{4.DIFA(TOF - ZERO) + DIFC^2}}.$$

$$(A2)$$

References

[1] Fullwood DT, Niezgoda SR, Adams BL, Kalidindi SR. Prog Mater Sci 2010;55:477.
[2] Rollett AD, Lebensohn RA, Groeber M, Choi Y, Li J, Rohrer GS. Model Simul Mater Sci 2010;18:074005.

[3] Brown DW, Holden TM, Clausen B, Prime MB, Sisneros TA, Swenson H, et al. Acta Mater 2011;59:864.
[4] Holden TM, Suzuki H, Carr DG, Ripley MI, Clausen B. Mater Sci Eng A – Struct 2006;437:33.
[5] Miller M, Bernier J, Park JS, Kazimirov A. Rev Sci Instrum 2005;76:113903.
[6] Miller MP, Park JS, Dawson PR, Han TS. Acta Mater 2008;56:3927.
[7] Oddershede J, Schmidt S, Poulsen HF, Sorensen HO, Wright J, Reimers W. J Appl Crystallogr 2010;43:539.
[8] Neil CJ, Wollmershauser JA, Clausen B, Tomé CN, Agnew SR. Int J Plast 2010;26:1772.
[9] Aydiner CC, Bernier JV, Clausen B, Lienert U, Tomé CN, Brown DW. Phys Rev B 2009;80:024113.
[10] Dawson P, Boyce D, MacEwen S, Rogge R. Mater Sci Eng A – Struct 2001;313:123.
[11] Dini D, Song X, Zhang SY, Korsunsky AM. J Strain Anal Eng 2009;44:55.
[12] Song X, Zhang SY, Dini D, Korsunsky AM. Comput Mater Sci 2008;44:131.
[13] Wong SL, Dawson PR. Acta Mater 2010;58:1658.
[14] Roters F, Eisenlohr P, Hantcherli L, Tjahjanto DD, Bieler TR, Raabe D. Acta Mater 2010;58:1152.
[15] Clausen B, Lorentzen T, Leffers T. Acta Mater 1998;46:3087.
[16] Clausen B, Tomé CN, Brown DW, Agnew SR. Acta Mater 2008;56:2456.
[17] Merkel S, Tomé C, Wenk HR. Phys Rev B 2009:79.
[18] Delannay L, Loge RE, Chastel Y, Van Houtte P. Acta Mater 2002;50:5127.
[19] Delannay L, Melchior M, Jacques PJ, Van Houtte P. Mater Sci Forum 2005;495–497:1627.
[20] Ritz H, Dawson PR. Model Simul Mater Sci 2009;17.
[21] Lebensohn RA. Acta Mater 2001;49:2723.
[22] Lebensohn RA, Brenner R, Castelnau O, Rollett AD. Acta Mater 2008;56:3914.
[23] Lebensohn RA, Kanjarla AK, Eisenlohr P. Int J Plast, in press. http://dx.doi.org/10.1016/j.ijplas.2011.12.005.
[24] Bourke MAM, Dunand DC, Ustundag E. Appl Phys A – Mater 2002;74:S1707.
[25] Clausen B, Lorentzen T, Bourke MAM, Daymond MR. Mater Sci Eng A – Struct 1999;259:17.
[26] Moulinec H, Suquet P. Cr Acad Sci Ii 1994;318:1417.
[27] Moulinec H, Suquet P. Comput Method Appl Mech 1998;157:69.
[28] Prakash A, Lebensohn RA. Model Simul Mater Sci 2009;17:064010.
[29] Lebensohn RA, Montagnat M, Mansuy P, Duval P, Meysonnier J, Philip A. Acta Mater 2009;57:1405.
[30] Asaro RJ, Needleman A. Acta Metall Mater 1985;33:923. Overview.42.
[31] Michel JC, Moulinec H, Suquet P. CMES – Comput Model Eng 2000;1:79.
[32] Michel JC, Moulinec H, Suquet P. Int J Numer Meth Eng 2001;52:139.
[33] Melchior MA, Delannay L. Comput Mater Sci 2006;37:557.
[34] Turner PA, Tomé CN. Acta Metall Mater 1994;42:4143.
[35] Oliver EC, Daymond MR, Withers PJ. Acta Mater 2004;52:1937.
[36] Dawson PR, Boyce DE, Rogge RB. Mater Sci Eng A – Struct 2005;399:13.
[37] Lienert U, Han T-S, Almer J, Dawson PR, Leffers T, Margulies L, et al. Acta Mater 2004;52:4461.
[38] Ribárik G, Gubicza J, Ungár T. Mater Sci Eng A – Struct 2004;387–389:343.
[39] Ungar T, Dragomir I, Revesz A, Borbely A. J Appl Crystallogr 1999;32:992.
[40] Ungar T, Ribarik G. Mater Sci Eng A – Struct 2010;528:112.
[41] Stokes AR. Proc Phys Soc Lond 1948;61:382.
[42] Balogh L, Capolungo L, Tomé C. Acta Mater 2012;60:1467.
[43] Kanjarla AK, Van Houtte P, Delannay L. Int J Plast 2010;26:1220.
[44] Kanjarla AK, Delannay L, Van Houtte P. Metall Mater Trans A 2011;42A:660.
[45] Ray A, Diak BJ. Scripta Mater 2010;62:606.
[46] Van Houtte P, Kanjarla AK, Van Bael A, Seefeldt M, Delannay L. Eur J Mech A – Solid 2006;25:634.
[47] Raveendra S, Kanjarla AK, Paranjape H, Mishra SK, Mishra S, Delannay L, et al. Metall Mater Trans A 2011;42A:2113.
[48] Hutchings MT, Withers PJ, Holden TM, lorentzen T. Introduction to the characterisation of residual stresses by neutron diffraction. London: CRC Press, Taylor & Francis; 2005.
[49] Clausen B. SMARTSware manual. Los Alamos National Laboratory Report LA-UR 04-6581; 2005.